FULL PAPER

Plasmonic Vortices

ADVANCED
OPTICAL
MATERIALS

www.advopticalmat.d

Check for
updates

Manipulating Terahertz Plasmonic Vortex Based on Geometric and Dynamic Phase

XiaoFei Zang, YiMing Zhu,* ChenXi Mao, WeiWei Xu, HongZhen Ding, JingYa Xie, QingQing Cheng, Lin Chen, Yan Peng, Qing Hu, Min Gu, and SongLin Zhuang

Electromagnetic waves carrying orbital angular momentum (OAM), namely, vortex beams, have a plethora of applications ranging from rotating microparticles to high-capacity data transmissions, and it is a continuing trend in manipulating OAM with higher degrees of freedom. Here, an approach to control terahertz (THz) near-field plasmonic vortex based on geometric and dynamic phase is proposed and experimentally demonstrated. By locally tailoring the orientation angle (geometric phase) and radial position (dynamic phase) of aperture arrays embedded in an ultrathin gold film, the excited surface waves can be flexibly engineered to form both spin-independent and spin-dependent THz plasmonic vortex field distributions, resulting in multi-degree of freedom for controlling OAM of THz surface plasmon polaritons (SPPs). Arbitrary OAM values of THz plasmonic vortex and coherent superposition between two OAM states are investigated based on near-field scanning terahertz microscopy (NSTM) system. The proposed approach provides unprecedented freedom to modulate THz near-field plasmonic vortex, which will have potential applications in THz communications and quantum information processing.

1. Introduction

Electromagnetic waves can carry angular momentum with two different components, that is, the spin angular momentum (SAM) and orbital angular momentum (OAM).[1] SAM is manifested as circularly polarized (CP) beam, where electric and

magnetic fields rotate continuously around the beam axis during propagation.[2] In contrast, electromagnetic waves transporting OAM (namely, vortex beam) is associated with helical phase structure, showing the doughnut-shaped field distribution.[3] A vortex beam has a helical wavefront described by $\exp(iq\phi)$, where ϕ is the azimuthal angle and q is the topological charge determined by the number of phase discontinuities within a 2π range. In theory, the OAM of electromagnetic waves can possess an infinite number of eigen modes ($q = 1, 2, 3....$) that can carry hitherto unprecedented quantities of data, leading to high-capacity free space data transmissions.[4,5] Free space vortex beam is also expected to have many applications such as trapping[6] and rotating microparticles.[7,8] They can be generated by various approaches, i.e., diffractive optical element,[9] spatial light modulators,[10,11] Pancheratnam-Berry phase optical element,[12] metasurfaces,[13–20] and photopatterned large birefringence liquid crystal.[21,22]

On the other hand, near-field OAM that is related to plasmonic vortex has attracted considerable attention due to its potential application in light focusing, optical tweezers, and ultrathin vortex plates. The methods of generating plasmonic vortex can be mainly classified into two categories. The former is circular slits or catenary structure[23–34] embedded in a metal film to generate plasmonic vortex or spin-Hall effect. The specific phase (geometric phase) distribution can be tailored by locally varying the orientation angle of each slit segment, and thus, the arbitrary OAM values of spin-independent vortex field distribution can be realized. However, OAM of electromagnetic waves in this case is just proposed in theory[25] with the same vortex field distribution and the reverses sign of OAM number for incident circular-polarized waves (the left circularly polarized (LCP) and right circularly polarized (RCP) electromagnetic waves, respectively). On the contrary, the latter is related to the dynamic phase induced by path difference along the azimuthal angle of chiral geometries, i.e., spiral and whirlpool-shaped slits.[35–38] But, the difference of plasmonic OAM between the LCP and RCP illuminations is always restricted to 2, limiting the OAM values of the excited surface waves (under the LCP or RCP illumination). Obviously, existing methods to generate plasmonic OAM encounter challenges

Prof. X. Zang, Prof. Y. Zhu, Dr. C. Mao, Dr. W. Xu, Dr. H. Ding,
Prof. J. Xie, Dr. Q. Cheng, Prof. L. Chen, Prof. Y. Peng, Prof. S. Zhuang
Terahertz Technology Innovation Research Institute, and Shanghai Key
Lab of Modern Optical System
University of Shanghai for Science and Technology
No. 516 JunGong Road, Shanghai 200093, China
E-mail: ymzhu@usst.edu.cn
Prof. Q. Hu
Department of Electrical Engineering and Computer Science
and Research Laboratory of Electronics
Massachusetts Institute of Technology
77 Massachusetts Avenue, Cambridge, MA 02139, USA
Prof. M. Gu
Laboratory of Artificial-Intelligence Nanophotonics
School of Science RMIT University Melbourne
Victoria 3000, Australia

The ORCID identification number(s) for the author(s) of this article
can be found under https://doi.org/10.1002/adom.201801328.

in the reverses sign of OAM number (based on geometric phase individually) and the restricted difference of plasmonic OAM (based on dynamic phase individually), which inevitably degrades the perceptive devices for on-chip applications, i.e., polarization multiplexing[34] and optical trapping.[39,40] Here, we propose an approach to control terahertz (THz) near-field plasmonic vortex and overcome the above limitations, by combining the geometric and dynamic phase. Indeed, it is a continuing trend in manipulating OAM with higher degrees of freedom. Thus, merging both the geometric and dynamic phase will yield unprecedented freedom for controlling OAM of THz surface plasmon polaritons (SPPs).

In this paper, a series of metasurfaces with predesigned double-ring distributed slit arrays are designed to investigate the manipulation of the THz near-field plasmonic vortex. We experimentally demonstrate that the geometric phase modulation induces spin-independent plasmonic vortex (field distribution) by locally tailoring the orientation angle of slit arrays. Then, we study the control of THz near-field THz OAM by combining geometric and dynamic phase (induced by shifting the spatial position of the slit array). In addition, the coherent superposition between two OAM states is discussed under the illumination of linear-polarized (LP) THz beam. The multi-degree of freedom for manipulating OAM of THz SPPs will open new avenues in controlling THz polarization multiplexing, communications, and fundamental physics.

2. Design and Methods

Figure 1 shows schematic of the designed structure for manipulating THz near-field plasmonic vortex. Two types of

metasurface-based lens are proposed in this paper: circular double-ring distributed slit arrays (Figure 1b) and Archimedes spiral slit arrays (Figure 1c). For the circular-shaped slit arrays (see Figure 1a, left), the topological charge of the plasmonic vortex is 2 (under LCP illumination), when the rotation angle of the slit in a turn is 1.5 times of 2π. When combining with both geometric and dynamic phase ($d_2 = \lambda_{SPP}$)), the corresponding OAM number is turned into 3, as shown in Figure 1a (middle). For LP illumination, both the LCP and RCP incident beams can excite near-field plasmonic vortex, and they can be coherently superimposed with each other, showing a quite different field distribution (Figure 1a, right). As a proof-of-concept, the geometric parameters of the slit arrays are selected as follows: $l = 300$ μm, $w = 130$ μm, $d_1 = 342$ μm, $d_2 = 684$ μm, $\rho_0 = 2736$ μm. The slit arrays with geometrical charge can be described in cylindrical coordinates (ρ, θ')

$$\rho(\theta) = \begin{cases} \rho_0 & \text{(circular-shaped structure)} \\ \rho_0 + m\dfrac{\lambda_{SPP}}{2\pi} \cdot \theta' & \text{(Archimedes spiral structure)} \end{cases} \quad (1)$$

where ρ_0 is the initial radius and λ_{SPP} represents the SPPs wavelength ($\lambda_{SPP} = \lambda\sqrt{\dfrac{\varepsilon_d + \varepsilon_m}{\varepsilon_m \varepsilon_d}}$, in which λ is the incident wavelength, and ε_d and ε_m are the permittivity of dielectric and metal, respectively). m is an integer ($m = \pm1, \pm2, \pm3...$), and $d_3 \approx d_4 \approx \dfrac{\lambda_{SPP}}{2}$. The rotated angle of each slit in the double-ring distributed arrays can be expressed as follows
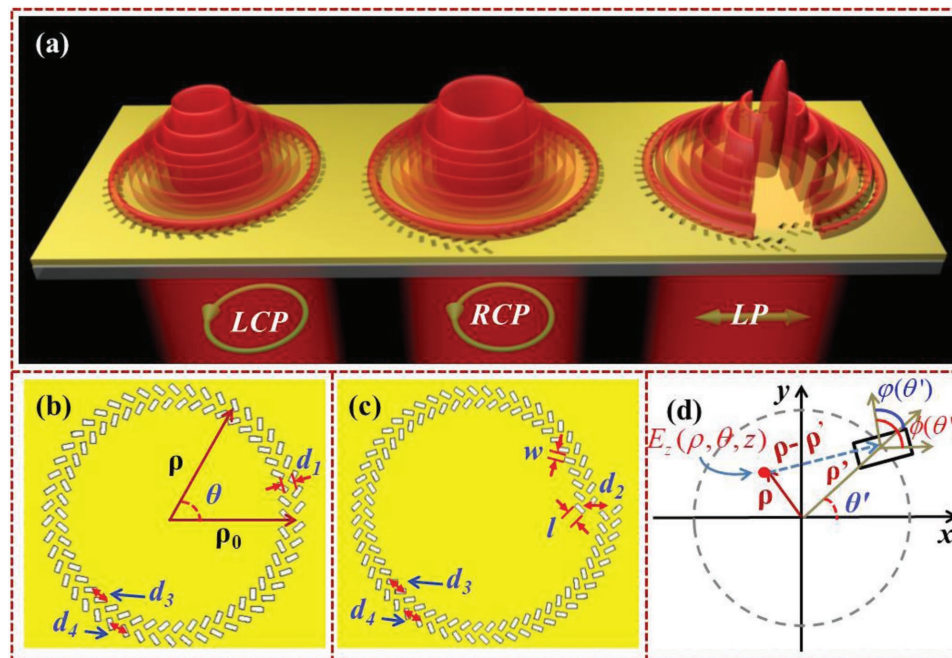

Figure 1. Schematic of control THz near-field plasmonic vortex: a) THz plasmonic OAM modulated with geometric phase (left), geometric and dynamic phase (middle), and the coherent superposition between two OAM states (right). b) and c) are the top view of the corresponding metasurfaces to control plasmonic vortex. d) Schematic for definitions of the structure parameters.

**ADVANCED
SCIENCE NEWS**

www.advancedsciencenews.com

**ADVANCED
OPTICAL
MATERIALS**

www.advopticalmat.de

$$\phi(\theta') = \begin{cases} \dfrac{3}{4}\pi + n\theta' & \text{(inner slit)} \\[2mm] \dfrac{1}{4}\pi + n\theta' & \text{(outer slit)} \end{cases} \tag{2}$$

where n is the slit-rotation factor.

Each slit (upon illumination) in the designed metasurface can serve as a dipole source (Figure 1d), and the excited SPPs (E_z field) inside the designed single-ring structure can be expressed by integrating dipole sources along the slit arrays[25]

$$E_z(\rho,\theta,z) = e^{-\alpha z}\int A(\theta')e^{\pm i\phi(\theta')}e^{ik_{SPP}|\bar\rho-\bar\rho'|}\mathrm{d}\theta' \tag{3}$$

where α is the attenuation coefficient of the SPPs mode and $\phi(\theta')$ is the rotation angle of the slit. $A(\theta') = A_0\cos\phi(\theta')$ is the amplitude of the dipole source and $\pm$ is determined by the LCP and RCP incidence, respectively. For the double-ring and orthogonal distributed slit array, the corresponding SPPs in the interface between metal and air can be written as

$$\begin{aligned} E_z(\rho,\theta) &= \int A(\theta')e^{\pm i\phi(\theta')}e^{ik_{SPP}|\bar\rho-\bar\rho'|}\mathrm{d}\theta' + \int A\left(\theta'+\frac{\pi}{4}\right)e^{\pm i\phi\left(\theta'+\frac{\pi}{4}\right)}e^{ik_{SPP}\lambda/2}e^{ik_{SPP}|\bar\rho-\bar\rho'|}\mathrm{d}\theta' \\ &= A_0\int(\cos((n-1)\theta')\pm i\sin((n-1)\theta'))\,e^{\pm in\theta'}e^{\pm im\theta'}\cdot e^{ik_{SPP}|\bar\rho-\bar\rho'|}\mathrm{d}\theta' \\ &= A_0\int e^{\pm i(2n-1)}e^{\pm im\theta'}\cdot e^{ik_{SPP}|\bar\rho-\bar\rho'|}\mathrm{d}\theta' \\ &\propto J_{m\pm(2n-1)}(k_{SPP}\rho) \end{aligned} \tag{4}$$

in which n is the slit-rotation factor which can be defined as the ratio between the rotation angle of the slit in a turn and 2π. Equation (4) yields a $q = m \pm (2n-1)$-order Bessel function,

where the parameter m is associated with the dynamic phase while n is connected with the geometric phase.

To verify our proposed approaches, we fabricate four samples to control the THz near-field plasmonic vortex (see **Figure 2**a–d) and explore the corresponding characteristics using the near-field scanning terahertz microscopy, as shown in Figure 2e. The sample is fabricated by conventional photolithography and magnetron sputtering coating. The substrate is polyimide with thickness of 25 µm and permittivity of $\varepsilon = 3.5 + 0.035i$. 150 nm thickness of the gold film with predesigned slit arrays is coating on the substrate. Here, dual-turn of the circular distributed slit array (and Archimedes spiral slit array) sample is designed and fabricated, and the SPPs excited at different turns have propagation phase differences of 2π, resulting in the constructively interfere of SPPs excited between different turns. Therefore, the multi-turn design will have stronger field enhancement than that of the case of single-turn. In experiment (see Figure 2e), the collimated THz waves radiated from a 100 fs ($\lambda = 780$ nm) laser pulse pumped photoconductive antenna emitter is modulated with a proper polarized state and then impinges on the sample. A commercial THz near-field probe mounted on a translation stage is used as the detector. The probe is located closely (≈ 50 µm) to the sample to collect spatial electric field and phase. Here, a microscope (FORTUNE TECHPLOGY FT-FH1080) is applied to identify the distance between the probe and metasurface. A mirror tip appears due to the smooth and flat surface of the sample, and we can approximately control/estimate the distance by moving the 3D translation stage. The 2D electric field distribution is detected in 50 µm step in the x- and y-directions.
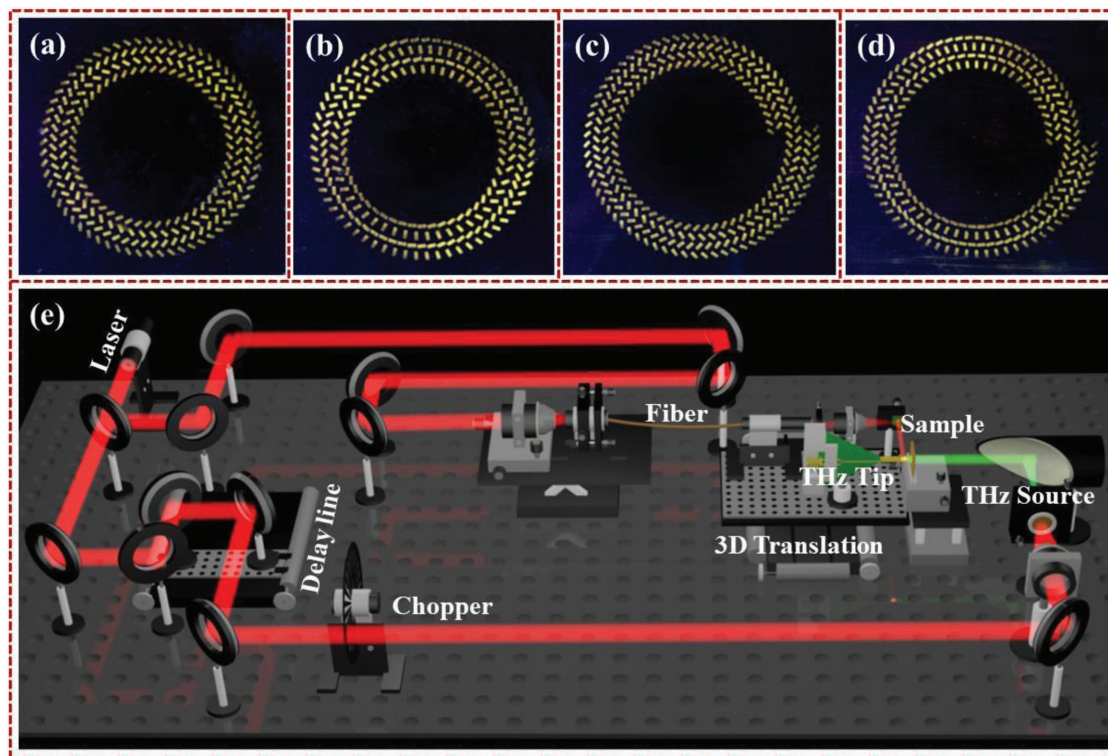

Figure 2. a)–d) The optical images of the designed plasmonic lens. e) Experiment set-up of the near-field scanning terahertz microscopy.

3. Results and Discussions

First, we study the geometric phase–induced THz near-field OAM manipulation and the coherent superposition between two OAM states (with reverse sign of OAM number), as shown in **Figure 3**. In this case, the slit-rotation factor is $n = 1$, which means that the rotation angle of the slit in a turn is 2π (see Figure 2a). The excited SPPs under the illumination of circular-polarized (LCP and RCP) THz waves can be expressed as

$$E_z(\rho,\theta) \propto \begin{cases} J_1(k_{SPP}\rho) & \text{(LCP)} \\ J_{-1}(k_{SPP}\rho) & \text{(RCP)} \end{cases} \qquad (5)$$

which corresponds to ±1-order Bessel function. The analytical electric fields ($|E_z|^2$) are illustrated in Figure 3a₁,a₃. Although, the topological charge of the plasmonic vortex are ±1 for LCP and RCP incident THz waves, respectively, both of them are identical in electric-field distribution, leading to the spin-independent and doughnut-shaped field distribution. However, the phase distributions are reversed with rotation direction counterclockwise and clockwise determined by the positive and negative topological charge (see Figure 3a₂,a₄). Here, each aperture embedded in the gold film can launch SPPs with a different initial phase induced by the orientation angle $\phi(\theta')$. The overall phase shift across a whole turn is $(2n-1)\sigma\pi = 2\pi$ ($n = 1$, $\sigma = \pm 1$), where "+" and "−" represent the sign of the phase shift for the incident LCP and RCP THz waves, respectively. The corresponding numerical simulations and experimental demonstrations for the incident frequency of $f = 0.33$ THz are shown in Figure 3b₁–b₄ and Figure 3c₁–c₄, respectively. Here, the finite integration time domain (FITD) solver (CST Microwave Studio) is used to calculate the field and phase distributions.

Conducting wall boundary condition is employed along the x- and y-directions while the open (add space) condition is used in the z-direction. The measured results are matched with numerical simulations and the analysis model, except for a slight discrepancy because of the fabrication error, the approximate condition of $d_3 \approx d_4 \approx \frac{\lambda_{SPP}}{2}$ (in theory,[25,29] the distance of two neighboring slits of the outer and inner ring array should meet the demands of $d_3 = d_4 = \frac{\lambda_{SPP}}{2}$), and the limited number of the slits. Both the LCP and RCP illuminations can excite the near-field THz vortex (E_z field) with different helical phase, and thus, the coherent superposition between these two OAM states are realized and shown in Figure 3a₅,a₆. An LP incident THz beam is composed of two orthogonal components with opposite helicity, and the excited SPPs (upon the illumination of LP THz waves) can be written as

$$E_z(\rho,\theta) \propto J_1(k_{SPP}\rho)e^{i\theta} + J_{-1}(k_{SPP}\rho)e^{-i\theta} \qquad (6)$$

The corresponding intensity of the coherent field can be expressed as

$$I_z(\rho,\theta) \propto \left(J_1(k_{SPP}\rho)e^{i\theta'} + J_{-1}(k_{SPP}\rho)e^{-i\theta'} \right) \\ \times \left(J_1(k_{SPP}\rho)e^{-i\theta'} + J_{-1}(k_{SPP}\rho)e^{i\theta'} \right) = 4J_1^2(k_{SPP}\rho)\sin^2\theta' \qquad (7)$$

where the illumination of THz waves is x-polarized. For the y-polarized (LP) THz waves, the intensity of SPPs is $I_z(\rho,\theta) \propto 4J_1^2(k_{SPP}\rho)\cos^2\theta'$. Therefore, two symmetrically distributed (along the y-axis) and crescent-shaped coherent field and symmetrically distributed phase are obtained, as shown in Figure 3a₅,a₆. The numerical simulations and the experimental measurements are demonstrated in Figure 3b₅–c₆, which are well agreed with the analysis model. Unlike the direct intensity superposition[34] (incoherent superposition) of OAM states
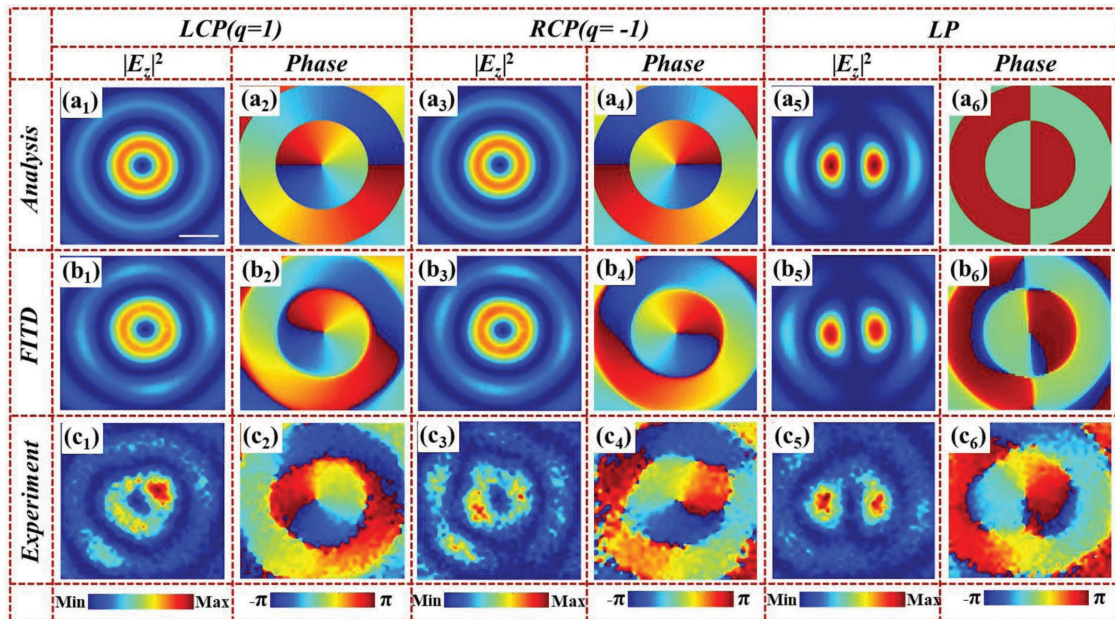

Figure 3. a₁–a₆) Analysis, b₁–b₆) numerical, and c₁–c₆) measured results of the electric field and phase distribution of THz plasmonic vortex with $m = 0$ and $n = 1$. The scale bar is 500 µm.
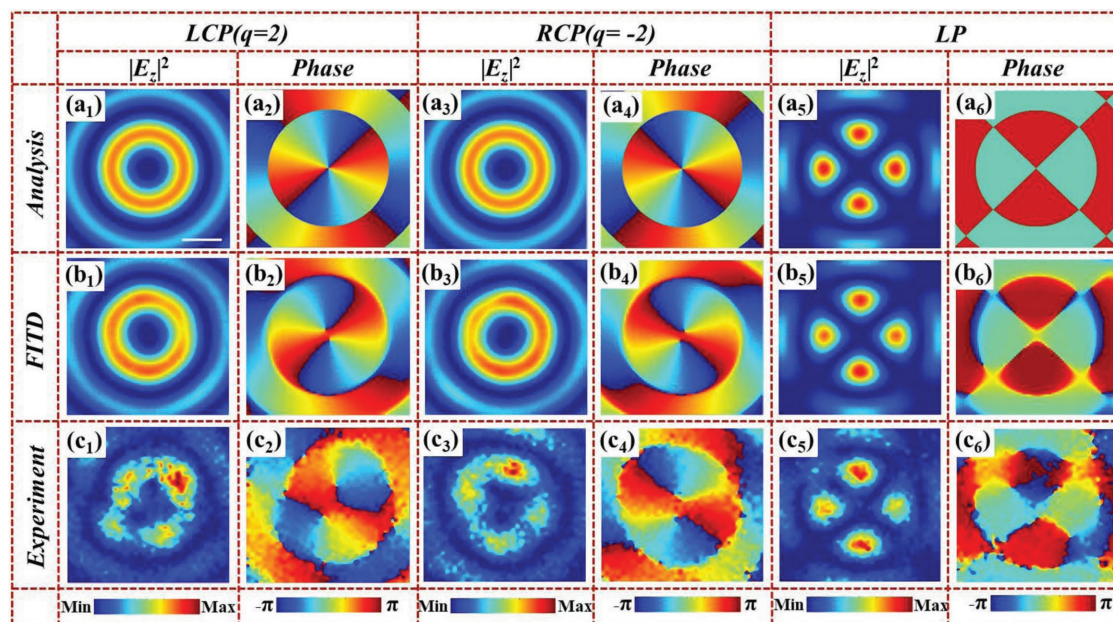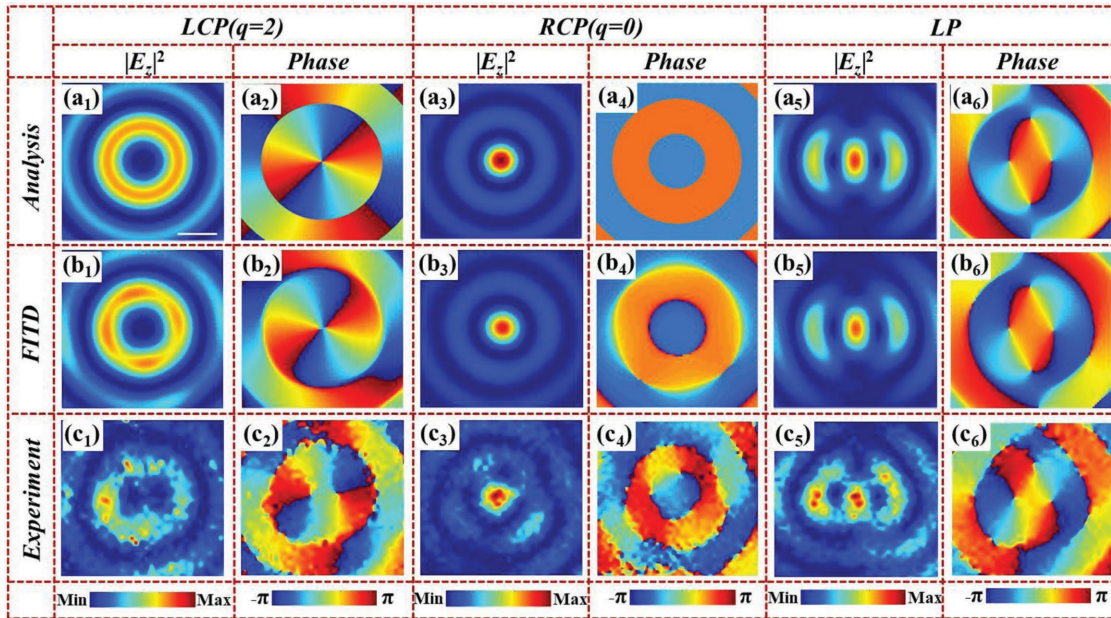
ADVANCED
SCIENCE NEWS
www.advancedsciencenews.com

ADVANCED
OPTICAL
MATERIALS
www.advopticalmat.de

Figure 4. a_1–a_6) Analysis, b_1–b_6) numerical, and c_1–c_6) measured results of the electric field and phase distribution of THz plasmonic vortex with $m = 0$ and $n = 1.5$. The scale bar is 500 μm.

in free space, the excited near-field vortex induced by LCP and RCP illuminations are coherent with each other, resulting in the coherent superposition between two OAM states.

To characterize the functionality of THz near-field OAM controlled by geometric phase, we further study the manipulation of plasmonic vortex with slit-rotation factor of $n = 1.5$, as shown in **Figure 4** (see Figure 2b for the sample). In this situation, the rotation angle of the slit in a turn is 3π that is 1.5 times of the azimuth angle. The topological charge of the excited plasmonic vortex is $q = \pm (2n-1) = \pm 2$ ($m = 0$), representing a doughnut-shaped field distribution and a larger radius of hollow fields in the center, as shown in Figure 4a_1,a_3. The excited SPPs can be expressed as $E_z(\rho,\theta) \propto J_{\pm2}(k_{SPP}\rho)$, corresponding to a two-order Bessel function. It should be noted that the intensity ($|E_z|^2$) of the plasmonic vortex is also spin-independent for both LCP and RCP illuminations. The spatial helical phase structure reveals two evident abrupt phase jumps from $-\pi$ to π (see Figure 4a_2,a_4). The numerical simulations and experimental measurements are depicted in Figure 4b_1–b_4 and Figure 4c_1–c_4, respectively, exhibiting excellent qualitative agreements with the analysis model (Figure 4a_1–a_4). The coherent superposition between ±2-order OAM states are illustrated in Figure 4a_5,a_6. The intensity of the coherent superposition can be expressed as $I_z(\rho,\theta) \propto 4 J_2^2(k_{SPP}\rho)\cos^2 2\theta'$ (for y-polarized illumination), leading to quadruple petal–shaped field distribution shown in Figure 4a_5. The corresponding phase profile is depicted in Figure 4a_6. The calculated (Figure 4b_5,b_6) and measured (Figure 4c_5,c_6) results are also well matched with the analysis model. Compared with the cases of $n = 1.5$ (Figure 4) and $n = 1$ (Figure 3), we can conclude that the THz near-field OAM can be well modulated with the geometric phase by tailing the orientation angle of slit arrays.

In addition to geometric phase, dynamic phase can also be applied to modulate the near-field plasmonic vortex. We investigate the manipulation of THz near-field OAM by combing geometric and dynamic phase shown in **Figure 5**. The designed structure is composed of Archimedes doubleing-ring slit arrays (see Figure 2c), in which the slit-rotation factor is $n = 1$, and the shifting of radial position in a turn is $d_2 = \lambda_{SPP}$ ($m = 1$). Figure 5a_1,a_3 shows the spin-dependent field distributions ($|E_z|^2$) of the sample under the incidence of LCP and RCP THz waves, respectively. For LCP illumination, a doughnut-shaped field distribution is appeared with the corresponding topological charge of $q = m + (2n-1) = 2$ (Figure 5a_1), and the phase shift across a turn is 4π (Figure 5a_2). When the polarization of the incident THz waves is switched from LCP to RCP, a hot spot (Figure 5a_3) is focusing in the center with topological charge of $q = m - (2n-1) = 0$, indicating the homogeneous phase distribution around a turn (Figure 5a_4). For LP incidence, the intensity and phase of the coherent superposition between these two OAM states ($q = 2$, $q = 0$) are shown in Figure 5a_5,a_6, respectively. The coherent field in this case is associated with $I_z(\rho,\theta) \propto (J_0^2(k_{SPP}\rho) + J_2^2(k_{SPP}\rho) + J_0 J_2(k_{SPP}\rho)\sin 2\theta')$, while the phase distribution does not linearly change with the azimuthal angle. All of the simulations and measurements are shown in Figure 5b_1–c_6, and show a good agreement with the analysis model.

To demonstrate the versatility of the proposed approach, a fourth metasurface (Figure 2d) that can realize different OAM states (compared with the third sample (Figure 2c)), is also developed. Now, the slit-rotation factor is $n = 1.5$, while the shifting of radial position in a turn is fixed as λ_{SPP} ($m = 1$). Therefore, the topological charge of the excited plasmonic vortex under the LCP illumination is $q = m + (2n-1) = 3$ (**Figure 6**a_1–c_1), and it is $q = m - (2n-1) = -1$ for the RCP incidence (Figure 6a_3–c_3). The phase distributions are also matched with the corresponding OAM states (see Figure 6a_2–c_2 and Figure 6a_4–c_4). The coherent superposition of field and phase distributions between these

ADVANCED
SCIENCE NEWS
www.advancedsciencenews.com

ADVANCED
OPTICAL
MATERIALS
www.advopticalmat.de

Figure 5. a_1–a_6) Analysis, b_1–b_6) numerical, and c_1–c_6) measured results of the electric field and phase distribution of THz plasmonic vortex with $m = 1$ and $n = 1$. The scale bar is 500 µm.

two OAM states are given in Figure 6a_5–c_5 and Figure 6a_6–c_6, exhibiting an in inhomogeneous intensity distributions and nonlinearly phase variation along the azimuthal direction.

4. Conclusion

In summary, we have analytically, numerically, and experimentally demonstrated an ultrathin metasurface approach to realize the manipulation of THz near-field OAM. The unique method lies in the combination of geometric and dynamic phase induced by engineering the orientation angle and the radial position of aperture arrays, respectively. By controlling the geometric and (or) dynamic phase, arbitrary topological charges of THz plasmonic vortex can be obtained with flexibility under the illumination of CP THz waves, leading to the multi-degree of freedom for manipulating OAM of THz SPPs. Unlike the direct intensity superposition of OAM states in free
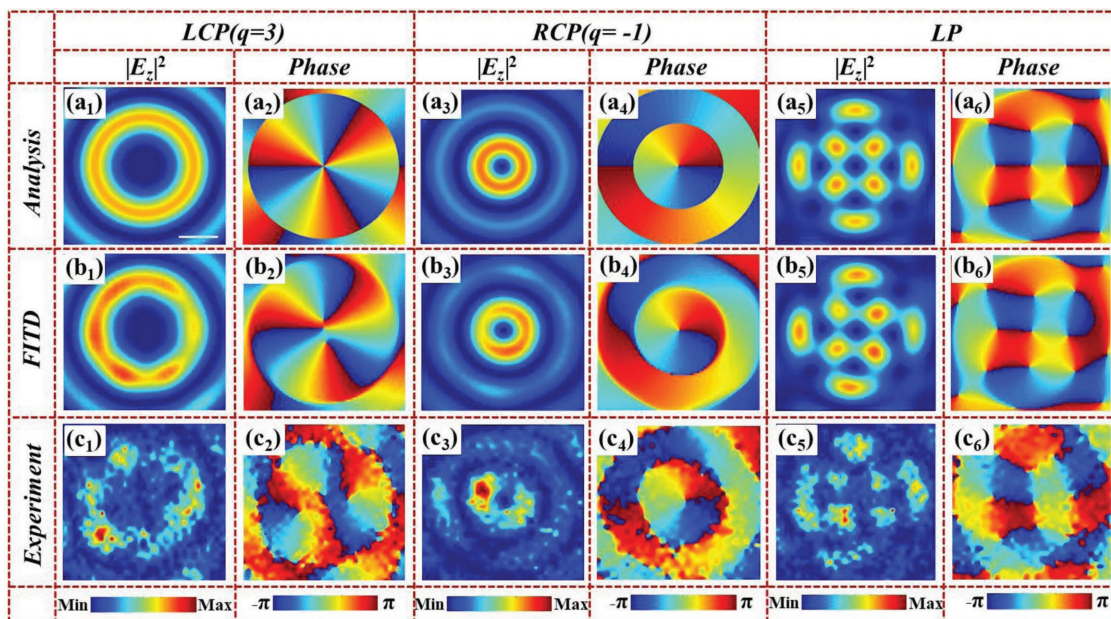

Figure 6. a_1–a_6) Analysis, b_1–b_6) numerical, and c_1–c_6) measured results of the electric field and phase distribution of THz plasmonic vortex with $m = 1$ and $n = 1.5$. The scale bar is 500 µm.

space, the superposition between two THz near-field OAM states is coherent with each other. Due to the simplicity of the design and its powerful control of the plasmonic vortex, the flexible method in this work may have practical applications in imaging, communication, and information processing.

Conflict of Interest

The authors declare no conflict of interest.

[1] L. Allen, S. M. Barnett, M. J. Padgett, *Optical Angular Momentum*, Institute of Physics Publishing, Bristol **2003**.

[2] J. F. Belintante, *Physica* **1940**, *7*, 449.

[3] L. Allen, M. W. Beijersbergen, R. J. C. Spreeuw, J. P. W oerdman, *Phys. Rev. A* **1992**, *45*, 8185.

[4] J. Wang, J. Y. Yang, I. M. Fazal, N. Ahmed, Y. Yan, H. Huang, Y. Ren, Y. Yue, S. Dolinar, M. Tur, A. E. Willner, *Nat. Photonics* **2012**, *6*, 488.

[5] Y. Yan, G. Xie, M. P. J. Lavery, H. Huang, N. Ahmed, C. Bao, Y. Ren, Y. Cao, L. Li, Z. Zhao, A. F. Molisch, M. Tur, M. J. Padgett, A. E. Willner, *Nat. Commun.* **2014**, *5*, 4876.

[6] M. E. J. Friese, J. Enger, H. Rubinsztein-Dunlop, N. R. Heckenberg, *Phys. Rev. A* **1996**, *54*, 1593.

[7] N. B. Simpson, K. Dholakia, L. Allen, M. J. Padgett, *Opt. Lett.* **1997**, *22*, 52.

[8] M. Friese, T. Nieminen, N. R. Heckenberg, H. Rubinsztein-Dunlop, *Nature* **1998**, *394*, 348.

[9] N. R. Heckenberg, R. Mcduff, C. P. Smith, *Opt. Lett.* **1992**, *17*, 221.

[10] K. D. Wulff, D. G. Cole, R. L. Clark, R. DiLeonardo, J. Leach, J. Cooper, G. Gibson, M. J. Padgett, *Opt. Express* **2006**, *14*, 4169.

[11] A. Jesacher, A. Schwaighofer, S. Furhapter, C. Maurer, S. Bernet, M. Ritsch-Marte, *Opt. Express* **2007**, *15*, 5801.

[12] G. Biener, A. Niv, V. Kleiner, E. Hasman, *Opt. Lett.* **2002**, *27*, 1875.

[13] N. Yu, P. Genevet, M. A. Kats, F. Aieta, J. P. Tetienne, F. Capasso, Z. Gaburro, *Science* **2011**, *334*, 333.

[14] L. Huang, X. Chen, H. Mühlenbernd, G. Li, B. Bai, Q. Tan, G. Jin, T. Zentgraf, S. Zhang, *Nano Lett.* **2012**, *12*, 5750.

[15] G, Li , M. Kang, S. Chen, S. Zhang, E. Y. B. Pun, K. W. Cheah, J. Li, *Nano Lett.* **2012**, *13*, 4148.

[16] J. Sun, X. Wang, T. Xu, Z. A. Kudyshev, A. N. Cartwright, *Nano Lett.* **2014**, *14*, 2726.

[17] M. Mehmood, S. Mei, S. Hussain, K. Huang, S. Siew, L. Zhang, T. Zhang, X. Ling, H. Liu, J. Teng, A. Danner, S. Zhang, C. Qiu, *Adv. Mater.* **2016**, *28*, 2533.

[18] F. Yue, D. Wen, J. Xin, B. D. Gerardot, J. Li, X. Chen, *ACS Photonics* **2016**, *3*, 1558.

[19] F. Yue, D. Wen, C. Zhang, B. D. Gerardot, W. Wang, S. Zhang, X. Chen, *Adv. Mater.* **2017**, *29*, 1603838.

[20] C. Zhang, F. Yue, D. Wen, M. Chen, Z. Zhang, W. Wang, X. Chen, *ACS Photonics* **2017**, *4*, 1906.

[21] S. Ge, P. Chen, Z. Shen, W. Sun, X. Wang, W. Hu, Y. Zhang, Y. Lu, *Opt. Express* **2017**, *25*, 12349.

[22] P. Chen, L. Ma, W. Duan, J. Chen, S. Ge, Z. Zhu, M. Tang, R. Xu, W. Cao, T. Li, W. Hu, Y. Lu, *Adv. Mater.* **2018**, *30*, 1705865.

[23] W. Chen, D. C. Abeysinghe, R. L. Nelson, Q. Zhan, *Nano Lett.* **2009**, *9*, 4320.

[24] N. Shitrit, I. Bretner, Y. Gorodetski, V. Kleiner, E. Hasman, *Nano Lett.* **2011**, *11*, 2038.

[25] S. Lee, S. Kim, H. Won, B. Lee, *IEEE Photonics Technol. Lett.* **2015**, *27*, 705.

[26] Q. Tan, Q. Guo, H. Liu, X. Huang, S. Zhang, *Nanoscale* **2017**, *9*, 4944.

[27] L. Huang, X. Chen, B. Bai, Q. Tan, G. Jin, T. Zentgraf, S. Zhang, *Light: Sci. Appl.* **2013**, *2*, e70.

[28] M. Pu, X. Li, X. Ma, Y. Wang, Z. Zhao, C. Wang, C. Hu, P. Gao, C. Huang, H. Ren, X. Li, F. Qin, J. Yang, M. Gu, M. Hong, X. Luo, *Sci. Adv.* **2015**, *1*, e1500396.

[29] J. Lin, J. P. B. Mueller, Q. Wang, G. Yuan, N. Antoniou, X. Yuan, F. Capasso, *Science* **2013**, *340*, 331.

[30] S. Xiao, F. Zhou, H. Liu, S. Zhu, J. Li, *Nat. Commun.* **2015**, *6*, 8360.

[31] S. T. Mei, K. Huang, H. Liu, F. Qin, M. Q. Mehmood, Z. G. Xu, M. Hong, D. Hua, J. Teng, C. W. Qiu, *Nanoscale* **2016**, *8*, 2227.

[32] X. Zang, F. Dong, F. Yue, C. Zhang, L. Xu, Z. Song, M. Chen, P. Chen, G. Buller, Y. Zhu, S. Zhuang, W. Chu, S. Zhang, X. Chen, *Adv. Mater.* **2018**, *30*, 1707499.

[33] L. Chen, Y. Wei, X. Zang, Y. Zhu, S. Zhuang, *Sci. Rep.* **2016**, *6*, 22027.

[34] L. Chen, N. Xu, L. Singh, T. Cui, R. Singh, Y. Zhu, W. Zhang, *Adv. Opt. Mater.* **2017**, *5*, 1600960.

[35] W. Chen, D. C. Abeysinghe, R. L. Nelson, Q. Zhan, *Nano Lett.* **2010**, *10*, 2075.

[36] R. Heeres, V. Zwiller, *Nano Lett.* **2014**, *14*, 4598.

[37] C. Chen, C. Ku, Y. Tai, P. Wei, H. Lin, C. Huang, *Nano Lett.* **2015**, *15*, 2746.

[38] H. Ren, X. P. Li, Q. M. Zhang, M. Gu, *Science* **2016**, *352*, 805.

[39] M. Righini, A. Zelenina, C. Girard, R. Quidant, *Nat. Phys.* **2007**, *3*, 477.

[40] W. Y. Tsai, J. S. Huang, C. B. Huang, *Nano Lett.* **2014**, *14*, 547.